

**A neoclassical calculation of toroidal rotation profiles
and comparison with DIII-D measurements**

W. M. Stacey, R. W. Johnson and J. Mandrekas*
Fusion Research Center
Georgia Institute of Technology
Atlanta, GA 30332 USA
January, 2006

Abstract

Momentum and particle balance and neoclassical viscosity were applied to calculate the radial profile of toroidal rotation velocity in several DIII-D [J. Luxon, Nucl. Fusion, 42, 614 (2002)] discharges in a variety of energy confinement regimes (Low-mode, Low-mode with Internal Transport Barrier, High-mode, and High-mode with Quiet Double Barrier). Calculated toroidal rotation velocities generally were found to (over-) predict measured values to well within a factor of 2.

*on leave at Office Fusion Energy Science, US Dept. Energy, Germantown, MD

PACS.52.55.Fi

I. Introduction

There have been longstanding experimental¹⁻¹⁰ and theoretical¹¹⁻²⁸ efforts to characterize and understand toroidal rotation and the related radial transport of angular momentum in neutral beam driven tokamaks. Since the theoretical expression for the toroidal rotation velocity follows directly from toroidal momentum balance once the viscous stress is specified, understanding toroidal rotation is primarily a matter of understanding toroidal viscosity (and any other torque input mechanisms).

It was early noted that the familiar “perpendicular” viscosity of classical theory was much too small to account for observed momentum damping^{1,13-15}, even when extended to take neoclassical effects into account^{13-15,18,19}, giving rise to the now widespread belief that momentum transport in tokamaks was “anomalous”. The observation in several recent experimental investigations^{4,5,7,8,10,29} that the ratio of the inferred momentum diffusivity and ion thermal diffusivity (χ_ϕ/χ_i), or the ratio of parameters that are determined by these diffusivities, was relatively uniform over the radial dimension of the plasma was interpreted as further evidence that the momentum transport was anomalous, since the ion thermal transport was believed to be anomalous in these discharges.

It was also early pointed out^{11,12} (but little noted) that there was a second, gyroviscous contribution to the radial transport of angular momentum in classical theory with a gyroviscosity coefficient that was several orders of magnitude larger than the perpendicular viscosity coefficient. The relative obscurity of the gyroviscous contribution in momentum transport analyses is perhaps due in part to the fact that it vanishes in cylindrical geometry (hence would not have survived in much of the early theoretical work) and in part by its puzzling failure to survive in some contemporary developments of neoclassical viscosity based on a formal gyroradius ordering of the flow fields^{18,19,26}, all of which essentially recovered the much smaller classical perpendicular viscosity with small corrections. In any case, unfamiliarity notwithstanding, there would now appear to be a firm theoretical basis for gyroviscosity^{11,12,16,17,20-25,27,28}. It is our purpose in this paper to test neoclassical viscosity by using neoclassical gyroviscosity to calculate the radial profile of toroidal rotation velocity and to use neoclassical parallel viscosity to calculate the poloidal rotation and the poloidal density and velocity

asymmetries that are needed to evaluate the gyroviscous torque, and to compare the result with measured values of toroidal rotation in a set of DIII-D discharges.

We anticipate that there may be other, non-classical momentum transport mechanisms present in DIII-D (and other) discharges (e.g. Ref. 30). However, since the particle motions and forces that give rise to classical and neoclassical transport are always present (trapped particle effects only in the appropriate collisionality regime), it is important to make a comparison of the predictions of neoclassical momentum transport theory with rotation measurements, if for no other reason than to establish the magnitude of the additional transport that must be accounted for by these other transport mechanisms.

For this purpose, we make use of the practical computation formalism that has been developed by extending the Braginskii gyroviscosity formalism to tokamak toroidal flux surface geometry¹⁷ (i.e. the “Pfirsch-Schluter” extension of classical gyroviscosity) and by developing a methodology for evaluating the poloidal asymmetry factors needed to determine the rate of radial transport of toroidal angular momentum²⁰. A number of previous, less extensive, comparisons of this formalism with experimental data³¹⁻³³ have established that gyroviscosity predicts the correct magnitude of the global momentum loss rate (the momentum confinement time) in many neutral beam driven tokamaks and under a variety of operating conditions. The intent of this paper is to extend these investigations to test the ability of this gyroviscosity formalism to predict the radial profile, as well as the overall magnitude, of the radial transport rate of toroidal angular momentum for neutral beam driven DIII-D plasmas in a variety of energy confinement regimes.

Radial momentum transport in tokamak plasmas is of intrinsic interest, of course, for what it reveals about basic transport processes. Moreover, toroidal rotation has also been shown to affect neoclassical particle transport^{34,35}, to suppress MHD resistive wall mode instabilities³⁶⁻³⁸, and to alter MHD equilibria³⁹, and is postulated to be involved in the shear suppression of transport enhancing microinstabilities⁴⁰.

II. Neoclassical Radial Transport of Toroidal Angular Momentum

A. Viscous torques

Following the previous generalization¹⁷ to toroidal flux-surface geometry of the Braginskii¹² derivation, the toroidal component of the viscous torque can be written

$$R^2 \nabla \phi \cdot \nabla \cdot \Pi = \frac{1}{Rh_p} \frac{\partial}{\partial l_\psi} (R^2 h_p \Pi_{\psi\phi}) + B_p \frac{\partial}{\partial l_p} \left(\frac{R \Pi_{p\phi}}{B_p} \right) \quad (1)$$

where the Π_{pq} are the stress tensor elements that result from the Braginskii decomposition of the rate-of-strain tensor extended to a right-hand ‘radial’, ‘poloidal’, toroidal (ψ, p, ϕ) flux-surface coordinate system with length elements $(dl_\psi = h_\psi d\psi, dl_p = h_p dp, dl_\phi = h_\phi d\phi)$. The viscous stress tensors have¹⁷ ‘perpendicular’ components

$$\Pi_{\psi\phi}^\perp = -\eta_2 R \frac{\partial}{\partial l_\psi} \left(\frac{V_\phi}{R} \right), \Pi_{p\phi}^\perp = -\eta_2 R \frac{\partial}{\partial l_p} \left(\frac{V_\phi}{R} \right) \quad (2)$$

gyroviscous components

$$\Pi_{\psi\phi}^{\text{gv}} = -\eta_4 R \frac{\partial}{\partial l_p} \left(\frac{V_\phi}{R} \right), \Pi_{p\phi}^{\text{gv}} = -\eta_4 R \frac{\partial}{\partial l_\psi} \left(\frac{V_\phi}{R} \right) \quad (3)$$

and ‘parallel’ viscous components

$$\Pi_{\psi\phi}^\parallel = 0, \Pi_{p\phi}^\parallel = -\frac{3}{2} \eta_0 f_p A_0 \quad (4)$$

where

$$A_0 = 2 \left\{ -\frac{1}{3} \left(\frac{\partial V_p}{\partial l_p} \right) + \left[\left(\frac{1}{R} \right) \frac{\partial R}{\partial l_p} + \frac{1}{3} \left(\frac{1}{B_p} \right) \frac{\partial B_p}{\partial l_p} \right] V_p + f_p R \frac{\partial \left(\frac{V_\phi}{R} \right)}{\partial l_p} \right\} \quad (5)$$

and $f_p = B_p / B_\phi$.

The Braginskii values of the viscosity coefficients in a collisional plasma are

$$\eta_0 \approx nT\tau, \eta_4 \approx nTm / ZeB = \eta_0 / \Omega\tau, \eta_2 \approx \eta_4 / \Omega\tau \approx \eta_0 / (\Omega\tau)^2 \quad (6)$$

where τ is the self-collision time and $\Omega = m / ZeB$ is the gyrofrequency. Since typically $\Omega\tau \approx 10^3 - 10^4$, $\eta_0 \gg \eta_4 \gg \eta_2$. Taking into account trapped particle effects that would occur at lower collisionality should not directly effect η_4 , which has no τ -dependence, and has been shown^{18,19} to have very little effect on η_2 . However, trapped particle effects at lower collisionality have a major effect on η_0 , which we represent as³⁴

$$\eta_{0j} = \frac{n_j m_j v_{thj} q R \varepsilon^{-3/2} v_{jj}^*}{(1 + \varepsilon^{-3/2} v_{jj}^*)(1 + v_{jj}^*)} \equiv n_j m_j v_{thj} q R f_j (v_{jj}^*) \quad (7)$$

where $v_{jj}^* = v_{jj} q R / v_{thj}$, v_{thj} is the thermal speed, q is the safety factor, and $\varepsilon = r / R$.

Since the flux surface average of the second term in Eq.(1) vanishes identically, and the ‘parallel’ component of the first term in Eq. (1) vanishes identically, the flux surface averaged toroidal viscous torque may be written as the sum of the gyroviscous and perpendicular viscous components

$$\langle R^2 \nabla \phi \cdot \nabla \cdot \Pi \rangle = \langle R^2 \nabla \phi \cdot \nabla \cdot \Pi \rangle_{gv} + \langle R^2 \nabla \phi \cdot \nabla \cdot \Pi \rangle_{\perp} \quad (8)$$

where

$$\langle R^2 \nabla \phi \cdot \nabla \cdot \Pi \rangle_{gv} = - \left\langle \frac{1}{Rh_p} \frac{\partial}{\partial l_\psi} \left(R^3 h_p \eta_4 \frac{\partial}{\partial l_p} (V_\phi / R) \right) \right\rangle \quad (9)$$

and

$$\langle R^2 \nabla \phi \cdot \nabla \cdot \Pi \rangle_{\perp} = - \left\langle \frac{1}{Rh_p} \frac{\partial}{\partial l_{\psi}} \left(R^3 h_p \eta_2 \frac{\partial}{\partial l_{\psi}} (V_{\phi}/R) \right) \right\rangle \quad (10)$$

If the plasma rotated as a rigid body, $\Omega \equiv V_{\phi}/R \neq \Omega(\psi, p)$, then both of these components of the viscous torque would vanish identically. It is departure from rigid body rotation in the flux surface, $\Omega = \Omega(p)$, that drives the gyroviscous torque, and departure from rigid body rotation radially, $\Omega = \Omega(\psi)$, that drives the perpendicular viscous torque. Although the radial departure of the toroidal rotation velocity from rigid body rotation is generally larger by an order of magnitude or more than the poloidal departure of the toroidal rotation velocity from rigid body rotation in the flux surface, the gyroviscosity coefficient is larger than the perpendicular viscosity coefficient by 3-4 orders of magnitude, $\eta_4 \approx (\Omega\tau)\eta_2 \approx (10^3-10^4)\eta_2$, so that the gyroviscous toroidal torque is generally a couple of orders of magnitude larger than the perpendicular toroidal viscous torque. We note again that it was the smaller, but more familiar, perpendicular toroidal viscous torque to which several authors were referring when they stated that the neoclassical viscosity is too small to account for experimentally observed rotation damping.

Finally, we further note that it has been suggested²³ that the above expression for the gyroviscous toroidal torque, which is based on the Braginskii development of the viscous stress tensor, may overestimate the momentum transport rate in regions of steep pressure gradients and low toroidal rotation (e.g. the plasma edge pedestal) because of the $V_{\phi} \sim v_{th}$ ordering of the Braginskii derivation¹². Mikhailovskii and Tsypin¹⁶ were the first, and Catto and Simakov²⁷ and Ramos²⁸ the most recent, to repeat the Braginskii derivation in the $V_{\phi} \ll v_{th}$ ordering. Braginskii's derivation, which is used in this paper, is valid if the fluid velocities in the directions perpendicular and parallel to \mathbf{B} are larger than the diamagnetic velocity and the diamagnetic velocity multiplied by B_{ϕ}/B_p , respectively²⁵. If this condition is not satisfied, then a heat flux term may be required also in the parallel, perpendicular and gyroviscous torque expressions^{25,27}. This 'large rotation' condition for the validity of the Braginskii ordering appears to be valid over most of the radius for the discharges considered in this paper, as will be discussed later.

B. *Toroidal viscous torque approximate representation*

In order to obtain an approximate model for numerically evaluating the gyroviscous torque on each flux surface separately, we specialize to toroidal geometry, use the representations $B = B^0/(1 + \varepsilon \cos \theta)$, $R = R_0(1 + \varepsilon \cos \theta)$, replace the radial gradients in Eq. (9) by radial gradient scale lengths (e.g. $L_n^{-1} = -1/n \partial n / \partial r$), and expand the poloidal dependence of densities and velocities in a low-order Fourier series of the form

$$n_j(r, \theta) = n_j^0 \left[1 + n_j^c(r) \cos \theta + n_j^s(r) \sin \theta \right] \quad (11)$$

to obtain a representation of the toroidal gyroviscous torque in terms of an angular momentum transfer, or “drag”, frequency, ν_{dj}

$$\left\langle R^2 \nabla \phi \cdot \nabla \cdot \boldsymbol{\pi}_j \right\rangle_{\text{gv}} \simeq \frac{1}{2} \tilde{\theta}_j G_j \frac{n_j m_j T_j}{e_j B_\phi} \frac{V_{\phi j}^0}{R} \equiv R n_j m_j \nu_{dj} V_{\phi j}^0 \quad (12)$$

where

$$\begin{aligned} \tilde{\theta}_j &\equiv (4 + \tilde{n}_j^c) \tilde{V}_{\phi j}^s + \tilde{n}_j^s (1 - \tilde{V}_{\phi j}^c) \\ &= (4 + \tilde{n}_j^c) \left(-(\hat{V}_{\theta j} / \hat{V}_{\phi j}) (\tilde{\Phi}^s + \tilde{n}_j^s) + \tilde{\Phi}^s \left(1 + (\hat{P}'_j / \hat{V}_{\phi j}) \right) \right) + \\ &\tilde{n}_j^s \left((\hat{V}_{\theta j} / \hat{V}_{\phi j}) (\tilde{\Phi}^c + \tilde{n}_j^c + 2) - \tilde{\Phi}^c \left(1 + (\hat{P}'_j / \hat{V}_{\phi j}) \right) \right) \end{aligned} \quad (13)$$

represents poloidal asymmetries and

$$G_j \equiv -\frac{r}{\eta_{4j} V_{\phi j}} \frac{\partial (\eta_{4j} V_{\phi j})}{\partial r} = r (L_n^{-1} + L_T^{-1} + L_V^{-1}) \quad (14)$$

represents radial gradients. We have used the gyroviscosity coefficient $\eta_{4j} \approx n_j m_j T_j / e_j B$ and introduced the notation

$$\widehat{V}_{\theta j} \equiv \frac{V_{\theta j}^0}{f_p \nu_{thj}}, \widehat{V}_{\phi j} \equiv \frac{V_{\phi j}^0}{\nu_{thj}}, \widehat{P}_j' \equiv \frac{1}{n_j^0 e_j B_\theta^0 \nu_{thj}} \frac{\partial \overline{p_j}}{\partial r},$$

$$f_p \equiv \frac{B_\theta}{B_\phi}, \widetilde{n}_j^{c/s} \equiv \frac{n_j^{c/s}}{\varepsilon}, \widetilde{\Phi}^{c/s} \equiv \frac{\Phi^{c/s}}{\varepsilon} = \frac{n_e^{c/s}}{\varepsilon (e\Phi/T_e)} \quad (15)$$

with the last relation following from electron momentum balance, and neglected radial gradients in the density asymmetry coefficients $n_j^{c/s}$. The radial gradient scale lengths needed to evaluate the G_j from Eq. (14) are taken from experiment in this paper. Φ is the electrostatic potential.

C. “Neoclassical” terminology and collisionality dependence of gyroviscosity

The terminology “neoclassical” is used differently by various authors, and the collisionality dependence of the neoclassical gyroviscosity is subtle, so a brief discussion of both is in order. Transport due to collisions in straight field-line geometry (e.g. cylinders) is referred to as “classical” transport. Kaufman¹¹ and Braginskii¹² worked out a “classical” theory of viscosity. In the more familiar case of Braginskii, the viscosity was derived from kinetic theory under the assumption of large collisionality and large rotation $V_\phi \sim \nu_{th}$.

Extension of “classical” Braginskii collisional transport to include the effects of toroidal geometry (i.e. Pfirsch-Schluter transport) is referred to in this paper, but not by all authors, as “neoclassical” transport. In general, collisional transport in toroidal geometry includes the “classical” transport plus the new Pfirsch-Schluter “neoclassical” transport effects due to the toroidal geometry. Since the latter effects are larger, the “classical” transport is usually neglected in toroidal geometry relative to the new Pfirsch-Schluter “neoclassical” transport, but it is still there (i.e. the forces producing it are still operable). Mikhailovskii and Tsypin¹⁶, Stacey and Sigmar¹⁷ and recently Catto and Simakov²⁷ extended “classical” viscosity theory to toroidal geometry to obtain what we refer to in this paper as a “neoclassical viscosity” theory that takes into account Pfirsch-Schluter-like toroidal geometry effects.

We note from Eq. (13) that this “Pfirsch-Schluter gyroviscosity” vanishes to leading order in the absence of an up-down asymmetry in either the density or the toroidal rotation velocity¹⁷, but survives at higher order²⁷. This does not mean that

gyroviscosity vanishes in a tokamak with an up-down symmetric magnetic field structure, because inertial and other effects can produce up-down density and rotation velocity asymmetries even in tokamaks with an up-down symmetric magnetic field structure^{20,31-33}. Catto and Simakov²⁷ recently concluded purely on theoretical grounds that sufficiently strong up-down asymmetries such as found in diverted plasmas could drive gyroviscous momentum transport rates comparable to those observed experimentally, but did not note that similarly strong up-down asymmetries could be produced by inertial and other effects (as our calculations will show).

At sufficiently small collisionality, trapped particle effects introduce additional transport effects in toroidal geometry that are usually larger than the Pfirsch-Schluter transport effects (at least for the more familiar heat conductivities), although the latter (and also the “classical” transport effects) are still present because most of the particles are untrapped. We refer to the transport associated with these trapped particle effects also as “neoclassical” transport, while noting that some authors refer to it as “banana-plateau” transport, and that yet other authors refer to only these trapped particle transport effects as “neoclassical”. Numerous authors have investigated trapped particle effects on the parallel component of the viscosity tensor and found them to cause a significant enhancement of the viscosity coefficient [Eq. (7) is one such example], but of course to exist only when the collisionality was small enough to allow a small number of trapped particles to execute trapped particle orbits. Hinton and Wong¹⁸ (and others) worked out the trapped particle effects on the perpendicular component of the viscosity and found only a small enhancement over the “classical” Braginskii value.

The Pfirsch-Schluter-like “neoclassical gyroviscosity” of this paper does not have any explicit collisionality dependence, and no one has suggested that there is any direct trapped particle effect on gyroviscosity, to our knowledge. This does not mean that the Pfirsch-Schluter-like gyroviscosity does not exist in low collisionality plasmas, only that trapped particle effects do not directly enhance gyroviscosity relative to the “neoclassical Pfirsch-Schluter” values produced by toroidal geometry effects. However, since trapped particle effects enhance the parallel component of viscosity [Eq. (7)] that is used in solving the poloidal momentum moments equations [Eqs. (19)-(22)] for the poloidal velocities and density asymmetries needed to evaluate the gyroviscous torque from Eqs.

(12)-(14), there is an indirect trapped particle collisionality dependence of gyroviscosity that is taken into account in the calculation of this paper.

D. Poloidal rotation velocities and density asymmetries

Evaluation of the poloidal asymmetry factors $\tilde{\theta}_j$ of Eq. (13) requires the solution of the poloidal momentum balance equations for the poloidal rotation velocities and the poloidal density asymmetries.

The poloidal component of the momentum balance equation is

$$n_j m_j \left[(\mathbf{V}_j \cdot \nabla) \mathbf{V}_j \right]_\theta + [\nabla \cdot \Pi_j]_\theta + \frac{1}{r} \frac{\partial p_j}{\partial \theta} - M_{\theta j} - F_{\theta j} + n_j e_j (V_{rj} B_\phi - E_\theta) = 0 \quad (16)$$

where the poloidal components of the inertial and viscous terms are

$$n_j m_j \left[(\mathbf{V}_j \cdot \nabla) \mathbf{V}_j \right]_\theta = n_j m_j \left[V_{rj} \frac{\partial V_{\theta j}}{\partial r} + \frac{V_{rj} V_\theta}{r} + \frac{1}{2} \frac{1}{r} \frac{\partial V_{\theta j}^2}{\partial \theta} + \frac{V_{\phi j}^2}{R} \sin \theta \right] \quad (17)$$

and

$$[\nabla \cdot \Pi_j]_\theta = \eta_{0j} \left(\frac{1}{2} A_{\theta j} \right) \left\{ \frac{1}{r} \frac{\partial \ln(\eta_{0j} A_{\theta j})}{\partial \theta} - 3 \frac{\sin \theta}{R} \right\} \quad (18)$$

and M and F represent external momentum input from the neutral beam injection and interspecies collisional friction, respectively. We note that the ‘‘parallel’’ component of the viscosity enters the rotation calculation at this point and ultimately affects the calculation of the poloidal asymmetry factors $\tilde{\theta}_j$ which enter into the calculation of the frequencies ν_{dj} for the radial transport of toroidal angular momentum.

Making expansions of the type indicated by Eq.(11) for the density and velocities for each species in Eq. (16) and taking the flux surface average with weighting functions 1, $\sin \theta$ and $\cos \theta$ results in a coupled set of moments equations (three times the number of ion species) that must be solved for the $V_{\theta j}^0$ and $\tilde{n}_j^{s,c}$ for all the plasma ion species. If the first term on the right in Eq. (17) is neglected, these equations can be solved locally on each radial flux surface. The justification for this neglect is the plausible assumption $V_{rj} \ll V_{\theta j} < V_{\phi j}$. The resulting equations are

$$\begin{aligned}
& \widehat{V}_{\theta_j} \left[-q \widehat{V}_{\phi_j} \varepsilon \left(\widetilde{n}_j^s + \widetilde{\Phi}^s \right) - q^2 f_j f_p \left(1 + \widetilde{\Phi}^c + \frac{2}{3} \widetilde{n}_j^c \right) + f_p \sum_{k \neq j} v_{jk}^* (1 + \Delta_{fric,j}) \right] \\
& - \sum_{k \neq j} \widehat{V}_{\theta k} \left[f_p v_{jk}^* \sqrt{\frac{m_j}{m_k}} \right] (1 + \Delta_{fric,k}) = \\
& - \widehat{V}_{r_j} (1 + \Delta_r) - q \varepsilon \frac{1}{4} \widetilde{n}_j^s - q \varepsilon \widehat{\Phi}_j \left[\frac{1}{4} (\widetilde{\Phi}^s + \Delta_{\Phi_j}) \right] - q^2 f_j f_p \left(\widehat{V}_{\phi_j} + \widehat{P}_j \right) \widetilde{\Phi}^c \\
& - q \varepsilon \widehat{V}_{\phi_j} \left[\left(\widehat{V}_{\phi_j} + \widehat{P}_j \right) \widetilde{\Phi}^s + \frac{1}{2} \widehat{V}_{\phi_j} \widetilde{n}_j^s \right]
\end{aligned} \tag{19}$$

where $\Delta_{fric,j} \equiv -\frac{1}{2} \varepsilon^2 \left(1 + n_j^c + (n_j^c)^2 + (n_j^s)^2 \right)$, $\Delta_{\Phi_j} \equiv \widetilde{n}_j^c \widetilde{\Phi}^s - \widetilde{n}_j^s \widetilde{\Phi}^c$, Δ_r is a higher order term that arises from the second term in Eq. (17), and

$$\begin{aligned}
& \widetilde{n}_j^s \left[\frac{1}{3} \frac{q^2}{\varepsilon} f_j f_p \widehat{V}_{\theta_j} + \frac{1}{2} \varepsilon \widehat{V}_{r_j} - \frac{1}{2} \varepsilon f_p \sum_{k \neq j} v_{jk}^* \widehat{V}_{\theta k} \sqrt{\frac{m_j}{m_k}} \right] \\
& + \widetilde{n}_j^c \left[\frac{1}{2} q f_p^2 \widehat{V}_{\theta_j}^2 - \frac{1}{4} q \right] = -\frac{1}{2} \varepsilon f_p \sum_{k \neq j} v_{jk}^* \widehat{V}_{\theta_j} \widetilde{n}_k^s - \frac{1}{2} q \widehat{V}_{\phi_j}^2 \\
& + \frac{1}{4} q \widehat{\Phi}_j \widetilde{\Phi}^c - \frac{q^2}{\varepsilon} f_j f_p \frac{1}{2} \left(\widehat{V}_{\theta_j} - \widehat{V}_{\phi_j} - \widehat{P}_j \right) \widetilde{\Phi}^s - \frac{1}{2} q f_p^2 \widehat{V}_{\theta_j}^2 + \Delta_{1,j}
\end{aligned} \tag{20}$$

where $\Delta_{1,j}$ is a collection of higher order terms calculated with a symbolic algebra routine, and

$$\begin{aligned}
& \widetilde{n}_j^c \left[\frac{1}{3} \frac{q^2}{\varepsilon} f_j f_p \widehat{V}_{\theta_j} + \frac{1}{2} \varepsilon \widehat{V}_{r_j} - \frac{1}{2} \varepsilon f_p \sum_{k \neq j} v_{jk}^* \widehat{V}_{\theta k} \sqrt{\frac{m_j}{m_k}} \right] \\
& + \widetilde{n}_j^s \left[-\frac{1}{2} q f_p^2 \widehat{V}_{\theta_j}^2 + \frac{1}{4} q \right] = -\frac{1}{2} \varepsilon f_p \sum_{k \neq j} \widetilde{n}_k^c \left[v_{jk}^* \widehat{V}_{\theta_j} \right] \\
& - \frac{1}{4} q \widehat{\Phi}_j \widetilde{\Phi}^s - \frac{q^2}{\varepsilon} f_j f_p \left[\frac{1}{2} \left\{ \left(1 + \widetilde{\Phi}^c \right) \widehat{V}_{\theta_j} - \left(\widehat{V}_{\phi_j} + \widehat{P}_j \right) \widetilde{\Phi}^c \right\} \right] \\
& + \Delta_{2,j}
\end{aligned} \tag{21}$$

where $\Delta_{2,j}$ is a collection of higher order terms calculated with a symbolic algebra routine. The $\tilde{V}_{\phi j}^{s,c}$ are derived from the radial component of the momentum balance equation and defined in Eq. (13) and in Eq. (25) below.. We note that $V_{\theta j}^c/V_{\theta j}^0 = -\varepsilon(1 + \tilde{n}_j^c)$ and $V_{\theta j}^s/V_{\theta j}^0 = -\varepsilon(\tilde{n}_j^s)$ have been derived from the particle continuity equations and used in the above development. We have introduced the additional notation

$$\hat{V}_{rj} \equiv \frac{\bar{V}_{rj}}{\left(\frac{m_j v_{thj}}{e_j B_\theta^0} \right) \left| f_p \right| \left(\frac{v_{thj}}{qR} \right)}, \quad v_{jk}^* \equiv \frac{\bar{v}_{jk}}{\frac{v_{thj}}{qR}}, \quad \hat{\Phi}_j \equiv \frac{e_j \bar{\Phi}}{T_j}, \quad (22)$$

The Δ_{xx} in Eqs. (19)-(21) are higher order terms that were not consistently retained in earlier versions (e.g. Ref. 24) of these equations.

E. Radial electric field and toroidal rotation velocities

For each ion species, the momentum balance equation minus $m_j \mathbf{V}_j$ times the particle balance equation is

$$n_j m_j (\mathbf{V}_j \cdot \nabla) \mathbf{V}_j + \nabla p_j + \nabla \cdot \Pi_j = -n_j e_j \nabla \Phi + n_j e_j \mathbf{V}_j \times \mathbf{B} + \mathbf{F}_j + \mathbf{M}_j \quad (23)$$

where $\mathbf{F}_j = -n_j m_j v_{jk} (\mathbf{V}_j - \mathbf{V}_k)$ is the interspecies collisional friction and \mathbf{M}_j is the net external momentum input (e.g. neutral beam input less any charge-exchange and asymmetric ionization source losses). The lowest-order radial component of the flux surface average of Eq. (23) for each species ‘j’ is

$$\left(\frac{\bar{E}_r}{B_\theta^0} \right) = V_{\phi j}^0 - \left(\frac{B_\phi^0}{B_\theta^0} \right) V_{\theta j}^0 + \bar{P}'_j + \bar{I}_j \quad (24)$$

where the overbar or zero superscript indicates the average value over the flux surface. If the inertial term is retained in the radial momentum balance, there is an additional term on the right in Eq. (24) $\bar{I}_j \equiv (m/e) \left((V_{\theta j}^0)^2 / r \right)$ but this term is generally higher order. We

will include it in the calculation of toroidal rotation velocities (Eq. (32)), but since it is not used to construct the “experimental” electric field we will not include it in the calculation of radial electric field for comparison with experiment.

The lowest-order radial component of the flux surface average of the $\sin\theta$ and $\cos\theta$ moments of Eq. (23) can be solved for the toroidal rotation asymmetry factors when an expansion $V_{\phi j}(r, \theta) = V_{\phi j}^0(r)(1 + V_{\phi j}^c \cos\theta + V_{\phi j}^s \sin\theta)$ is made

$$\begin{aligned}\tilde{V}_{\phi j}^c &= 1 - \left(\frac{\widehat{V}_{\theta j}}{\widehat{V}_{\phi j}} \right) \left(\tilde{\Phi}^c + \tilde{n}_j^c + 2 \right) + \tilde{\Phi}^c \left(1 + \frac{\widehat{P}_j'}{\widehat{V}_{\phi j}} \right) \\ \tilde{V}_{\phi j}^s &= \left(\frac{\widehat{V}_{\theta j}}{\widehat{V}_{\phi j}} \right) \left(\tilde{\Phi}^s + \tilde{n}_j^s \right) + \tilde{\Phi}^s \left(1 + \frac{\widehat{P}_j'}{\widehat{V}_{\phi j}} \right)\end{aligned}\quad (25)$$

where $\tilde{V}_{ij}^{s,c} = V_{ij}^{s,c} / \varepsilon$. The lowest-order radial component of the flux surface average of the $\sin\theta$ and $\cos\theta$ moments of Eq. (23) for the electrons can be solved for electrostatic potential asymmetry factors when a similar expansion is made

$$\tilde{\Phi}^{c/s} \equiv \frac{\Phi^{c/s}}{\varepsilon} = \frac{n_e^{c/s}}{\varepsilon(e\Phi^0/T_e)} \quad (26)$$

The flux surface average of the toroidal component of Eq. (23) for each species ‘j’ can be written

$$n_j^0 m_j \bar{v}_{jk} \left((1 + \beta_j) V_{\phi j}^0 - V_{\phi k}^0 \right) = n_j^0 e_j E_{\phi}^A + e_j B_{\theta}^0 \Gamma_j + \bar{M}_{\phi j} \equiv n_j^0 m_j \bar{v}_{jk} y_j, \quad (27)$$

where radial transport of toroidal momentum is represented by the parameter

$$\beta_j \equiv \frac{\bar{v}_{dj} + \nu_{nj} + S_{nbj}/n_j^0}{\bar{v}_{jk}} \quad (28)$$

where S_{nbj} is the local neutral beam source rate, which arises because of use of the continuity equation in evaluating the inertial term, and the gyroviscous angular momentum transport frequency, ν_{dj} , is defined by Eq. (12) and the inertial angular momentum transport frequency, ν_{nj} , is defined by

$$\begin{aligned}
\left\langle R^2 \nabla \phi \cdot n_j m_j (\mathbf{V}_j \cdot \nabla) \mathbf{V}_j \right\rangle &\approx \frac{1}{2} \left(\frac{V_{rj}}{R_o} \left\{ \varepsilon \left(1 + \tilde{n}_j^c + \tilde{V}_{\phi j}^c \right) - 2 R_o L_{v\phi, j}^{-1} \right\} - \right. \\
\varepsilon \frac{V_{\theta j}^0}{R_o} &\left. \left\{ \tilde{V}_{\phi j}^s \left(1 + \tilde{n}_j^c + \tilde{V}_{\theta j}^c \right) - \tilde{V}_{\theta j}^s \left(1 + \tilde{V}_{\phi j}^c \right) - \tilde{V}_{\phi j}^c \tilde{n}_j^s \right\} \right) n_j m_j R V_{\phi j}^0 \equiv R n_j m_j v_{nj} V_{\phi j}^0
\end{aligned} \tag{29}$$

The ion-electron friction term has been neglected. A sum over other species ‘k’ is implied and the collisional momentum conservation requirement $n_j^0 m_j \bar{v}_{jk} = n_k^0 m_k \bar{v}_{kj}$ has been used in deriving Eq. (27).

We note that most neoclassical derivations (e.g. Refs. 14 and 27) obtain the result that the radial electric field is proportional to the radial ion temperature gradient (which is proportional to V_o in those derivations). The above equations can be rearranged to compare with these earlier derivations. Using the radial momentum balance Eqs. (24) (but dropping the inertial terms) in the toroidal momentum balance Eqs.(27) to eliminate the $V_{\phi j}^0$ and summing over species yields another expression for the radial electrostatic field

$$\frac{\bar{E}_r}{B_\theta^0} = \frac{\left[\left\{ \widehat{M}_{\phi I} + \widehat{M}_{\phi i} \right\} + \beta_i \left\{ \bar{P}'_i - \left(\frac{B_\phi^0}{B_\theta^0} \right) (V_{\theta i}^0) \right\} + \beta_I \left\{ \bar{P}'_I - \left(\frac{B_\phi^0}{B_\theta^0} \right) (V_{\theta I}^0) \right\} \right]}{[\beta_i + \beta_I]} \tag{30}$$

that displays the dependence on momentum input, pressure and poloidal rotation velocity. Since earlier derivations usually do not take into account the presence of external angular momentum input they naturally do not obtain the terms in the first { } brackets.

III. Comparison with DIII-D rotation measurements

The main purposes of this paper are to compare theoretical and experimental toroidal rotation velocity radial profiles and to draw some conclusions therefrom about how much of the radial transport of toroidal angular momentum in DIII-D tokamak plasmas is accounted for by neoclassical viscosity (as represented in the previous section) and how much must be attributed to other processes. A diverse set of discharges including L- and H-modes, with and without internal transport barriers and with and without neon injection, were analyzed for this purpose, as indicated in Table 1. A secondary purpose was to extend the investigation of the effect of neon impurity injection on momentum transport, for which purpose three ‘‘sister shot’’ pairs with and without neon injection were included.

A. *Description of discharges*

L-mode "sister shots" 98777 and 98775 @ 1.6s⁴¹

These were L-mode shots that were operated identically in every respect except for the injection of 2.8% neon impurity concentration in shot 98775. Long wavelength turbulence as well as heat and momentum transport were measured to be reduced with neon-injection. The intrinsic carbon concentrations were 1.1% in #98777 and 0.5% in the neon-injected #98775. (The cited carbon and neon concentrations correspond to the measured values at $\rho = 1/2$ in this and other shots.)

L-mode ITB "sister shots" 102942 and 102940 @ 1.4s⁴²

These were co-injected shots with an internal transport barrier (ITB) and a typical L-mode edge. The measured temperature and toroidal velocity profiles were quite peaked throughout the discharge. The density profiles were flat early in the discharge, but sharp density and electron temperature gradients developed later in the discharge following an increase in beam power, indicating the formation of an internal transport barrier (ITB). The shots were operated identically except for neon injection in shot 102940, which produced broader profiles and higher temperatures (i.e. better energy confinement), larger toroidal rotation velocities, and reduced turbulence levels in the core as compared to the sister shot 102942 without neon injection.

H-mode shot 99411 @ 1.8s⁴³

This was a high-performance ($H_{89P} = 2.8$, $\beta_{NH_{89P}} = 10$) ELMing H-mode shot with a typical H-mode edge pedestal and a relatively large (5%) carbon intrinsic impurity concentration.

H-mode QDB "sister shots" 106919 @ 3.5s & 106972 @ 2.9s⁴⁴

These were counter-injected, quiescent double barrier (QDB) shots with both an internal transport barrier and an edge transport barrier typical of H-mode discharges. The edge was quiescent [i.e. free of edge localized modes (ELMs)], but a saturated coherent

MHD edge harmonic oscillation (EHO) was present at the separatrix. The turbulence was reduced but not entirely suppressed in the internal transport barrier. These discharges had relatively low plasma densities and large and accumulating concentrations of Ni and Cu (Z_{eff} at $\rho = 1/2$ was 4.1 @ 2010 ms and 5.4 @ 3510 ms, more than half of which was due to Ni and Cu). The carbon concentration was 3.7% in 106919 and 3.1% in 10697. The shots were operated identically except for neon injection in shot 106972.

B. “2-Species” calculation model

The calculation model consisted of Eqs. (19)-(21) for the poloidal rotation velocities and density asymmetries for the main ion (deuterium) and an effective impurity ion species, the two Eqs. (27) for the toroidal rotation velocities for the main and effective impurity ion species, and the radial component Eq. (27) of the momentum balance for the effective impurity species. We add the two toroidal momentum balance Eqs. (24) to obtain one relation between the deuterium and impurity ion rotation velocities

$$\beta_i V_{\phi i}^0 + \beta_I V_{\phi I}^0 = y_i + y_I \quad (31)$$

and then subtract the radial momentum balance Eqs. (24) for the deuterium ion and effective impurity ion species to obtain a second relation

$$V_{\phi i}^0 - \left(\frac{B_{\phi}^0}{B_{\theta}^0} \right) V_{\theta i}^0 + \bar{P}_i + I_i = V_{\phi I}^0 - \left(\frac{B_{\phi}^0}{B_{\theta}^0} \right) V_{\theta I}^0 + \bar{P}_I + I_I \quad (32)$$

The radial electric field then calculated from the radial momentum balance Eq. (24) for either the effective impurity species (consistent with the way the experimental radial electric field was calculated) or the main deuterium ion species were identical.

C. Evaluation of input parameters

We took the electron density distribution, the ion and electron temperature distributions, the toroidal electric field, and the radial gradient scale lengths L_n^{-1} , L_T^{-1} and L_v^{-1} from experiment. The radial distribution of neutral beam angular momentum

deposition was calculated with the code NBEAMS⁴⁵. The value of the electrostatic potential Φ used in Eq. (19) to calculate the poloidal rotation velocity was taken from TRANSP calculations⁴⁶ based on an integration inward of the experimental radial electric field. The calculation was only made out to $\rho = 0.9$ or 0.95 because atomic physics effects (not taken into account in the calculation) become an important momentum transfer mechanism closer to the separatrix.

A brief discussion of the use of the experimental radial gradient scale lengths L_n^{-1} , L_T^{-1} and L_v^{-1} is in order at this point so that their effect on the calculation is clear. Our intent in this paper is to test the validity of Eq. (9) and its approximate representation Eq. (12), the expression for the gyroviscous torque which determines the rate of radial transport of toroidal angular momentum. The radial derivatives enter Eq. (12) via the factor G_j . We are not able at this time to accurately calculate the radial distributions of n , T and V_ϕ needed to accurately evaluate G_j , yet the accurate evaluation the G_j is a necessary (but not sufficient) condition for Eq. (12) to predict the correct momentum transport rate. So we use the experimental gradient scale lengths to insure that an accurate evaluation of G_j is used to test Eq. (12). To put it another way, to calculate the correct momentum transport rate it is not only necessary to use the correct G_j , but also that the equation it is used in is the correct equation; e.g., if Eq. (10) for the perpendicular viscosity with $\eta = \eta_2 = \left(nmT / ZeB \right) / \Omega \tau$ was used instead of Eq. (9) to represent the radial transport of toroidal angular momentum, and if the same experimental radial gradient scale lengths were used to evaluate the expression equivalent to Eq. (12) derived from Eq. (10), the resulting magnitude of the toroidal rotation velocity would be several orders of magnitude larger because $\Omega \tau \approx 10^3 - 10^4$.

In a similar vein, we have elected to use the value of the electrostatic potential Φ calculated in TRANSP by integrating the experimental radial electric field, rather than integrating the calculated radial electric field, because there is some ambiguity about the boundary conditions that should be used.

D. Modeling of multiple impurity species

Since the present model is limited (by implementation, not inherently) to two ion species—“main ion” and “impurity”—it was necessary to model the six charge states of

carbon as a single impurity species with effective charge and mass determined by density weighting. This should be a good approximation over most of the plasma where carbon is fully ionized, but not in the edge. When neon was present it was similarly treated, and then the effective neon and carbon species were combined into a single effective impurity species. In the counter-injected shots with significant Cu and Ni impurities a similar treatment was used to obtain a single high-Z (Ni+Cu) impurity that was then combined with carbon and neon to obtain a single effective impurity species. Clearly, the association of the calculated “impurity” rotation velocity with the measured carbon VI rotation velocity in the presence of neon and high-Z impurities is valid only to the extent that the various impurity ion species are entrained by interspecies collisions to have a common rotation velocity, which is thus an implicit (and probably not very good) assumption of this model. We plan to introduce a multiple impurity species model in future work. Note that the less collisional main (deuterium) ions are not assumed to have the same rotation velocities as the more collisional impurity ions.

E. Numerical solution

Taking Eqs. (19)-(21) (for each species) and Eqs. (31)-(32) as our model for a two-species plasma of ions and impurities, we have an 8-dimensional system of coupled nonlinear equations at each radial mesh point. We solved this set of nonlinear equations for the rotation velocities and poloidal density coefficients $(V_{\phi i}, V_{\phi I}, V_{\theta i}, V_{\theta I}, n_i^c, n_I^c, n_i^s, n_I^s)$ at each spatial location numerically, using standard procedures based on the simplex search algorithm^{47,48} to minimize a scalar residual merit function defined as the magnitude of the sum of the normalized root-mean-square residuals for the individual equations at that spatial location. A convergence tolerance of $O(10^{-5})$ on the final step size in the change in the solution vector was used to define solutions, except as noted in the following section.

In general, more than one solution was found that satisfied this convergence criterion (depending on the initial trial solution), as is to be expected for a coupled set of non-linear equations and an unrestricted search algorithm. Solutions with scalar residuals up to a few percent (the estimated inaccuracy of the equations due to ancillary modeling approximations and input data uncertainties) were accepted. In some cases solutions

were accepted at isolated radial locations with a somewhat larger scalar residual when they were an obvious continuation of the solution at nearby radial locations with smaller scalar residuals. The most physically plausible solution meeting these criteria was selected as the physical solution.

F. Comparison of calculated and measured toroidal rotation velocities

The measured and calculated toroidal rotation frequencies are compared in Figs. 1-7. The calculated velocities are for the deuterium main ion species and for an effective impurity species, while the measured rotation velocity is for carbon VII. We generally found that the calculated deuterium velocity was somewhat greater than the calculated impurity velocity in the center, but that the difference diminished with radius. The calculated impurity species rotation velocity should be compared with the experimental carbon VII rotation velocity.

For the L-mode shots in Figs. 1 and 2, the two calculated velocities were similar (except in the very center) and the calculated impurity velocity was in quite good agreement with the measured values over the entire minor radius. Since only carbon impurity was present in shot 98777 and this impurity was fully ionized over most of the radius the single impurity species approximation should be valid, and the comparison of $V_{\phi I}$ and $V_{\phi C}^{\text{exp}}$ an unambiguous test of the theory within the uncertainty introduced by geometric and other ancillary modeling approximations and the uncertainty in the input experiment density and temperature data. With shot 98775, the necessity (at this stage in the development of the calculation model) of treating neon and carbon as a single impurity species introduces an additional ambiguity into the comparison of $V_{\phi I}$ and $V_{\phi C}^{\text{exp}}$, which may account for the calculated impurity velocity falling below the measured carbon VII velocity in the center.

For the L-mode shots with an ITB (just inside $\rho = 0.4$) in Figs. 3 and 4, the calculated velocities for the impurity species were similar to those for deuterium except inside the location of the ITB, and generally in agreement with the measured values to within less than a factor of two (over-prediction) at all radii. The same remarks made above about the single impurity species approximation apply also to this pair of shots.

For the H-mode shot in Fig. 5 the calculated carbon velocity was in quite good agreement (slight over-prediction) at all radii with the measured carbon VII velocity, and

the calculated deuterium velocity was larger than the calculated carbon velocity. Since carbon was the only impurity present, the comparison of $V_{\phi I}$ and $V_{\phi C}^{\text{exp}}$ provides an unambiguous test of the theory within the uncertainty introduced by geometric and other ancillary modeling approximations and the uncertainty in the input experiment density and temperature data.

For the lower density, counter-injected QDB shots with both an H-mode edge and an ITB, it was not possible to find solutions with a convergence tolerance of $O(10^{-5})$ on the change in the final step size of the solution vector, and this tolerance was relaxed to $O(10^{-3})$ in order to obtain solutions. Even with this tolerance, the solutions were outside the physically reasonable range $|n_{i,I}^{c,s}| < 1$ except in the center region for shot 106919, and these density asymmetries were also implausibly large but less than unity in magnitude in shot 106972. The calculated deuterium velocities were significantly greater than the calculated impurity velocities at all but the outermost radii, and the calculated impurity velocity was generally about a factor of 2 larger than the measured carbon VII velocity. We attribute this behavior to a breakdown in the ancillary “one effective impurity species” approximation in which carbon, neon and several charge states of copper and nickel (the latter contributing about half the $Z_{\text{eff}} \approx 4$) were lumped together as a single impurity species. Even with these difficulties in the impurity representation model, agreement between calculated impurity and measured carbon VI velocities was within a factor of about three. We note that differences in trace impurity toroidal velocities have been measured and calculated (using Eq. (32) but for two trace impurities) in DIII-D⁴⁹.

In the “sister shot” pair of L-mode shots that differed only by neon injection (98777 and 98775), both the measured and calculated rotation velocities were greater for the shot with neon injection, indicating an improvement in both calculated and measured momentum confinement with neon injection. For the other “sister shot” pairs with internal transport barriers (102942 and 102940) and with both internal and external transport barriers (106919 and 106972), the improvement of experimental confinement, if any, was less evident and the calculated rotation velocities were relatively insensitive to the neon injection.

In general, the agreement between calculated and measured velocities was quite good, and could certainly be characterized as being “well within a factor of two” if we exclude the 106xxx shots in which the impurity modeling appeared to be breaking down. This leads us to conclude that neoclassical theory can predict radial transport of toroidal angular momentum to well within a factor of two in DIII-D. The general observation of over-prediction is probably indicative that a different momentum transport mechanism (in addition to neoclassical) was also involved in the experiments, although refinements in the neoclassical viscosity model and improvements in the ancillary geometric and other modeling approximations could well account for this modest disagreement.

G. Comparison of poloidal rotation velocities

It is instructive to examine some of the intermediate quantities that are calculated from the poloidal momentum balance Eqs. (19)-(21) in order to evaluate the gyroviscous momentum transport frequency of Eq. (12), namely the poloidal velocities and poloidal asymmetry coefficients. The calculated profiles for the deuterium and impurity (carbon) ions poloidal rotation are shown for shot 98777 in Fig. 8a, together with the measured poloidal rotation profile for carbon VII (here designated $V_{\theta C}^{\Phi}$). The similarity in radial profile for the two calculated rotation velocities was also found for the other shots, except for the lower density 106xxx pair in which a greater difference was found. We note that the measured values do not include newly identified corrections for geometry and atomic physics effects, which can significantly affect the reported values for the measured poloidal velocities.

H. Radial electric fields

The radial electric field predicted using calculated rotation velocities and experimental pressure profiles to evaluate Eq. (24) (without the inertial term) are compared in Fig. 8b for shot 98777 with the ‘experimental’ electric field similarly calculated using the measured rotation velocities and pressure profile for carbon VI. The calculated profile for deuterium used the calculated main ion (deuterium) velocities and measured deuterium pressure profile, while the calculated profile for the impurity species used the calculated velocities for the effective impurity species and the measured carbon VI pressure profile. The calculated and measured values of the radial electric field are in relatively good agreement, with the disagreement arising from the difference in

calculated and measured poloidal velocity profiles. Similar, and sometimes better, agreement was found for the other shots, except for the 106xxx shots (in which the single effective impurity model seemed to break down).

I. Poloidal density and velocity asymmetries

The calculated “in-out” (cosine) and “up-down” (sine) density asymmetries for shot 98777 are shown in Figs. 8c and 8d. The general trends and magnitudes shown in these figures were also found for the other shots, except for the 106xxx shots in which the in-out density asymmetries became larger than unity, indicating a breakdown of the single effective impurity model. The calculated “in-out” density asymmetries increased with radius up to about 15% for the impurity ions (carbon in this shot) and $< 5\%$ for the deuterium ions. The calculated “in-out” toroidal rotation frequency asymmetries ($\Omega_j^c = V_{\phi_j}^c - \varepsilon$) were similar for deuterium and impurity ions and increased with radius up to -15% . The calculated “up-down” asymmetries were smaller, on the order of 10^{-5} over much of the minor radius, except for the impurity density coefficient which increased up to a few times 10^{-4} at the outer radii. The other shots were similar, except that n_I^c increased only to about 5% for shots 98775 and 99411 but to about 30% for the ITB shots 10294x, and $|n_{i,I}^c| > 1$ for shots 106xxx, which latter is unphysical.

We note that the toroidal rotation frequency is frequently assumed to be poloidally uniform in theoretical developments. These calculations indicate that this assumption could introduce errors on the order of as much as 15% in DIII-D.

IV. Summary and Conclusions

A self-consistent, first-principles formulation of rotation theory based on momentum balance and neoclassical viscosity and its implementation into a calculation model was described and then applied to calculate toroidal rotation velocity profiles in several DIII-D shots in different confinement regimes. The agreement between calculated and measured toroidal rotation velocities was well within a factor of two (except in two shots in which an ancillary approximation of the computation model broke down and the agreement was only to within a factor of about three), and the experimentally observed enhancement of momentum confinement with neon injection

was predicted for a pair of L-mode shots. The general trend of over-prediction of measured toroidal velocities is attributed to a combination of the need for refinements in the neoclassical viscosity representation, ancillary approximations in the calculation model, or to the presence in the experiment of an additional “anomalous” momentum transport or torque input mechanism not included in the calculation model. Future work will address these possibilities.

ACKNOWLEDGEMENT: This work was supported the U. S. Dept. of Energy Grant DE-FG02-00-ER54538 with the Georgia Tech Research Corporation. The authors are is grateful to the members of the DIII-D Team who made the measurements presented in this paper.

References

1. S. Suckewer, H. P. Eubank, R. J. Goldston, *et al.*, Phys. Rev. Lett., 43, 207 (1979).
2. R. C. Isler, L. E. Murray, E. C. Crume, *et al.*, Nucl. Fusion, 23, 1017 (1983).
3. R. J. Groebner, W. Pfeiffer, F. P. Blau, *et al.*, Nucl. Fusion, 26, 543 (1986).
4. S. D. Scott, V. Arunasalam, C. W. Barnes, *et al.*, Phys. Fluids B, 2, 1300 (1990).
5. H. P. L. deEsch, D. Stork and H. Weisen, Proc. Conf. Control. Fusion & Plasma Heating (Amsterdam), vol 14B, Part I (Geneva: Euro. Phys. Soc.) p90 (1990).
6. F. Wagner, F. Ryter, A. R. Field, *et al.*, Proc. 13th Int. Conf. Plasma Phys. Control. Fusion Res., Washington (Vienna: Int. Atomic Energy Agency) p277 (1991).
7. K-D. Zastrow, *et al.*, Proc. 22nd Euro. Conf. Control. Fusion Plasma Phys. (Bournemouth) vol 19C, part II (Geneva: Euro. Phys. Soc.) p453 (1995).
8. J. S. deGrassie, *et al.*, Proc. 26th Euro. Conf. Control. Fusion Plasma Phys. (Maastricht) vol 23J (Geneva: Euro. Phys. Soc.) p1189 (1999).
9. K-D. Zastrow, W. G. F. Core, L-G. Erickson, *et al.*, Nucl. Fusion, 38, 257 (1998).
10. J. S. deGrassie, D. R. Baker, K. H. Burrell, *et al.*, Nucl. Fusion, 43, 142 (2003).
11. A. N. Kaufmann, Phys. Fluids, 3, 610 (1960).
12. S. I. Braginskii, Rev. Plasma Phys., 1, 205 (1965).
13. M. N. Rosenbluth, P. H. Rutherford, J. B. Taylor, *et al.*, Proc. Conf. Plasma Phys. Control. Fusion (Vienna: Int. Atomic Energy Agency) vol. 1, p495 (1971).
14. R. D. Hazeltine, Phys. Fluids, 17, 961 (1974).
15. K. T. Tsang and E. A. Frieman, Phys. Fluids, 19, 747 (1976).
16. A. B. Mikhailovskii and V. S. Tsypin, Sov. J. Plasma Phys., 10, 51 (1984).
17. W. M. Stacey and D. J. Sigmar, Phys. Fluids, 28, 2800 (1985).
18. F. L. Hinton and S. K. Wong, Phys. Fluids, 28, 3082 (1985).
19. J. W. Connor, S. C. Cowley, R. J. Hastie and L. R. Pan, Plasma Phys. Control. Fusion, 29, 919 (1987).
20. W. M. Stacey, Phys. Fluids B, 4, 3302 (1992).

21. R. D. Hazeltine and J. D. Meiss, "Plasma Confinement", Addison-Wesley, Reading MA (1994), pp 208, 220 and 226.
22. A. L. Rogister, Phys. Plasmas, 1, 619 (1994).
23. H. A. Claassen, H. Gerhauser and A. Rogister, Phys. Plasmas, 7, 3699 (2000).
24. W. M. Stacey, Phys. Plasmas, 8 158 (2001); 9, 3874 (2002); and 11, 3096 (2004).
25. P. J. Catto and A. N. Simakov, Phys. Plasmas, 11, 91 (2004); also, Contrib. Plasma Phys., 44, 83 (2004).
26. S. K. Wong and V. S. Chan, Phys. Plasmas, 11, 3432 (2004).
27. P. J. Catto and A. N. Simakov, Phys. Plasmas, 12, 012501 (2005).
28. J. J. Ramos, Phys. Plasmas, 12, 112301 (2005).
29. D. Nishijima, A. Kallenbach, S. Gunter, et al., Plasma Phys. Control. Fusion, 47, 89 (2005).
30. A.G. Peeters and C. Angioni, Phys. Plasmas 12, 072515 (2005).
31. W. M. Stacey and D. R. Jackson, Phys. Fluids B, 5, 1828 (1993).
32. W. M. Stacey and M. Murakami, Phys. Plasmas, 8, 4450 (2001).
33. W. M. Stacey and J. Mandrekas, Phys. Plasmas, 9, 1622 (2002).
34. W. M. Stacey, A. W. Bailey, D. J. Sigmar and K. C. Shaing, Nucl. Fusion, 25, 463 (1985); W. M. Stacey and D. J. Sigmar, Phys. Fluids, 27, 2076 (1984) and 22, 2000 (1979); and Nucl. Fusion, 19, 1665, (1979).
35. K. H. Burrell, T. Ohkawa and S. K. Wong, Phys. Rev. Lett., 47, 511 (1981).
36. A. Bondeson and D. J. Ward, Phys. Rev. Lett., 72, 2709 (1994).
37. M. S. Chu, J. M. Greene, T. H. Jensen, R. W. Johnson, *et al.*, Phys. Plasmas, 2, 2236 (1995).
38. A. M. Garofalo, M. S. Chu, E. D. Fredrickson, *et al.*, Nucl. Fusion, 41, 1171 (2001).
39. E. Hameiri, Phys. Plasmas, 5, 3270 (1998).
40. K. H. Burrell, Phys. Plasmas, 4, 1499 (1997).
41. G. R. McKee, M. Murakami, J. Boedo, G. L. Jackson *et al.*, Phys. Plasmas, 7, 1870 (2000); Nucl. Fusion, 41, 317 (2001).
42. E. J. Doyle, C. M. Greenfield, M. E. Austin, *et al.*, Nucl. Fusion, 42, 333 (2002).
43. M. Murakami, H. St. John, T. A. Caspar, *et al.*, Nucl. Fusion, 40, 1257 (2000).

44. W. P. West, M. R. Wade, C. M. Greenfield, *et al.*, Phys. Plasmas, 9, 1970 (2002).
45. J. Mandrekas, "Physics models and user's guide for the neutral beam module of the SUPERCODE", Georgia Tech Fusion report GTFR-102 (1992), available from National Technical Information Service, NTIS-PB93-121887INZ.
46. R. J. Goldston, "Topics in confinement analysis of tokamaks with auxiliary heating," in *Basic Physical Processes of Toroidal Fusion Plasmas* (Commission of the European Comm. and Monotypia Frachi Citta di Castello, Italy, 1985), Vol 1, EUR 10418 EN.
47. W. H. Press, "Numerical Recipes", Cambridge Univ. Press, Cambridge (1992).
48. T. Rowan, "Functional Stability Analysis of Numerical Algorithms", PhD Thesis, Dept. Computer Sciences, University of Texas at Austin (1990).
<ftp://www.netlib.org/opt/>
49. L. R. Baylor, K. H. Burrell, R. J. Groebner, *et al.*, Phys. Plasmas, 11, 3100 (2004).

Table 1 Parameters of DIII-D shots selected for rotation analysis

Shot (time)	Conf. Mode	P _{nbi} (MW)	\bar{n} ($10^{19}/\text{m}^3$)	n_{carb}/n_e	$\left(n_{neon}/n_e\right)$	$\left(n_{ni,cu}/n_e\right)$	T_{i0}, T_{e0} (keV)	τ_E^{exp} (ms)
98777 1.6s	L	4.5 CO	3.4	0.011	-----	-----	3.5,2.5	66
98775 1.6s	L	4.5 CO	4.1	0.005	0.028	-----	6.3,3.3	90
99411 1.8s	H	9.2 CO	4.8	0.050	-----	-----	8.3,3.9	168
106919 3.5s	H- QDB	9.3 CTR	2.8	0.037	-----	0.005	14.2,4.2	140
106972 2.9s	H- QDB	8.7 CTR	2.9	0.031	0.003	0.003	15.2,4.2	117
102942 1.4s	L- ITB	7.0 CO	2.9	0.016	-----	-----	12.0,4.7	94
102940 1.4s	L- ITB	7.0 CO	3.2	0.006	0.013	-----	9.7,4.1	128

Figure Titles

1. Comparison of calculated and measured toroidal rotation velocities for L-mode shot 98777 without neon.
2. Comparison of calculated and measured toroidal rotation velocities for L-mode shot 98775 with neon.
3. Comparison of calculated and measured toroidal rotation velocities for L-mode shot 102942 with ITB but without neon.
4. Comparison of calculated and measured toroidal rotation velocities for L-mode shot 10940 with ITB and with neon.
5. Comparison of calculated and measured toroidal rotation velocities for H-mode shot 99411.
6. Comparison of calculation and measured toroidal rotation velocities for H-mode QDB shot 106919 without neon.
7. Comparison of calculation and measured toroidal rotation velocities for H-mode QDB shot 106972 with neon.
8. Intermediate calculated quantities for L-mode shot 98777: a) poloidal rotation velocities; b) radial electric field; c) “in-out” poloidal asymmetry coefficients; d) “up-down” poloidal asymmetry coefficients.

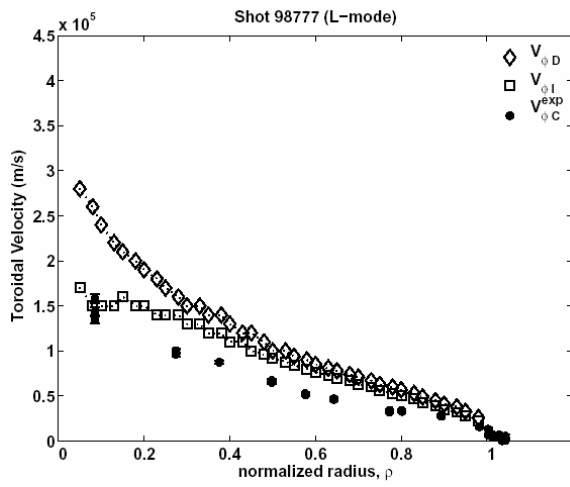


Figure 1

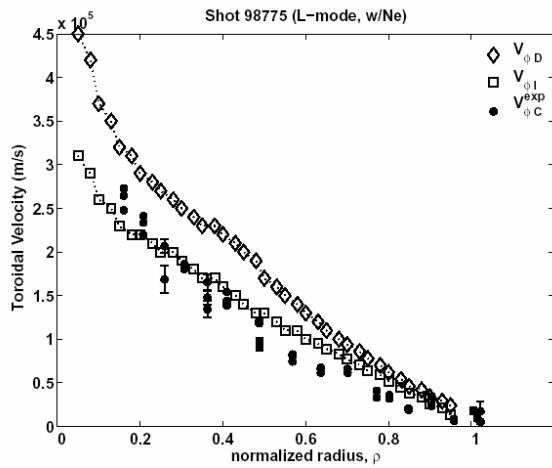


Figure 2

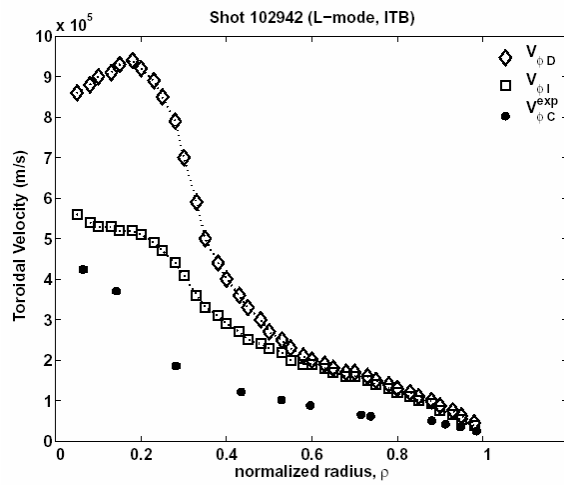


Figure 3

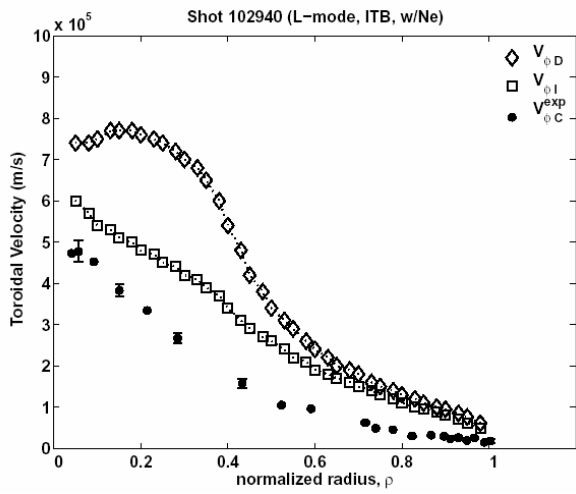


Figure 4

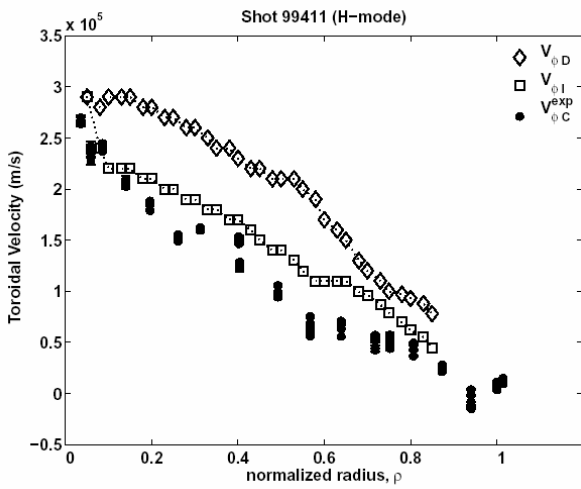


Figure 5

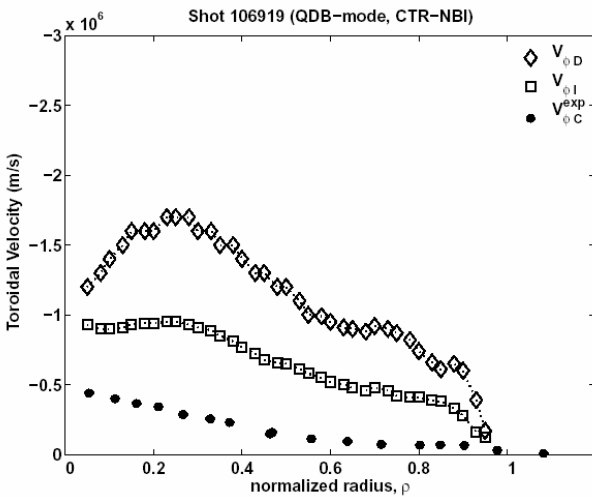


Figure 6

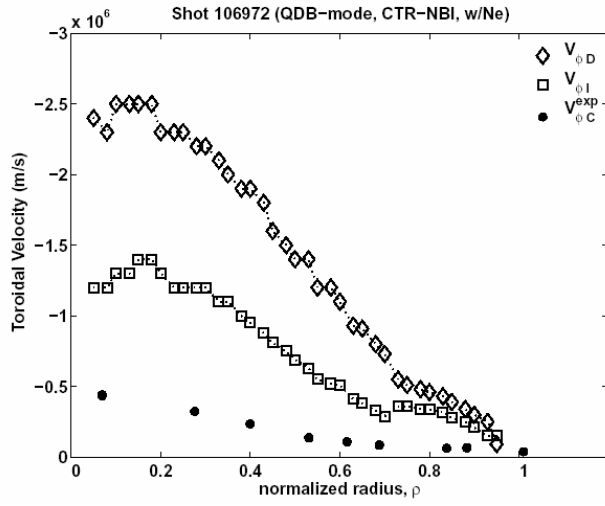


Figure 7

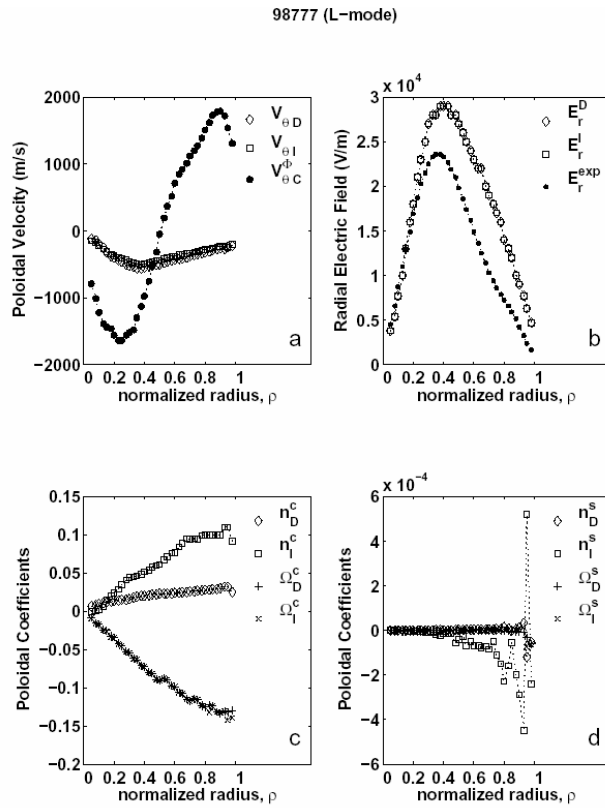


Figure 8